An integral non-intrusive electrochemical and in-situ optical technique for the study of the effectiveness of corrosion inhibition

Homborg, A. M.; Olgiati, M.; Denissen, P. J.; Garcia, S. J.

DOI
10.1016/j.electacta.2021.139619

Publication date
2022

Document Version
Final published version

Published in
Electrochimica Acta

Citation (APA)
Homborg, A. M., Olgiati, M., Denissen, P. J., & Garcia, S. J. (2022). An integral non-intrusive electrochemical and in-situ optical technique for the study of the effectiveness of corrosion inhibition. *Electrochimica Acta*, *403*, Article 139619. https://doi.org/10.1016/j.electacta.2021.139619

Electrochimica Acta 403 (2022) 139619

Contents lists available at ScienceDirect

Electrochimica Acta

journal homepage: www.elsevier.com/locate/electacta

An integral non-intrusive electrochemical and in-situ optical technique for the study of the effectiveness of corrosion inhibition

A.M. Homborg[a,b,*], M. Olgiati[c], P.J. Denissen[c], S.J. Garcia[c]

[a] Netherlands Defence Academy, Het Nieuwe Diep 8, 1781 AC Den Helder, the Netherlands
[b] Department of Materials Science and Engineering, Delft University of Technology, Mekelweg 2, 2628 CD Delft, the Netherlands
[c] Novel Aerospace Materials group, Faculty of Aerospace Engineering, Delft University of Technology, Kluyverweg 1, 2629 HS Delft, the Netherlands

ARTICLE INFO

Article history:
Received 12 October 2021
Revised 16 November 2021
Accepted 16 November 2021
Available online 29 November 2021

Keywords:
Corrosion inhibition
Electrochemical noise
Time-frequency analysis
In-situ optics
Combined electrochemical-optical analysis

ABSTRACT

This work investigates an integrated analysis of in-situ optical data and time-frequency information from electrochemical potential noise (EPN) data to study the effectiveness and durability of an anodic and cathodic corrosion inhibitor. Two different corrosion inhibiting species, cerium(III) (Ce(III)) and phytic acid (PHA), are tested on aluminum alloy AA2024-T3. Corrosion of AA2024-T3 serves as a negative reference. Time-frequency analysis of EPN data provides a direct insight in the kinetics of the electrochemical processes related to different types of corrosion and/or inhibitor activity over time. The simultaneous, in-situ optical technique allows visualizing and quantifying the surface changes associated with the electrochemical signals. Both Ce(III) and PHA were not capable to inhibit corrosion to a large extent, as re-immersion led to electrochemical (corrosion) activity for both inhibitors. Time-variant changes between corrosion, inhibitor activity, inhibited state and re-activation can effectively be discriminated from each other.

1. Introduction

One of the greatest challenges currently in the field of corrosion inhibition is the replacement of Cr(VI) in protective coatings. Ever since the late 1970s, researchers are investigating effective Cr(VI) substitutes [1]. The quest for finding suitable alternatives is full of obstacles, partly because the corrosion characteristics of high-strength aluminum alloys such as AA2024-T3 are not straightforward in the first place. These properties have therefore been studied quite extensively: the requirements for the high-strength mechanical properties of AA2024-T3 implicate a microstructure that contains second-phase particles, leading to such complex corrosion behavior [2–6]. In unprotected conditions, AA2024-T3 is highly vulnerable to degradation due to corrosion. Therefore protective species, or inhibitors, serve to actively protect the alloy [7]. The most common of these is the aforementioned Cr(VI), which is very effective, but also toxic and carcinogenic. Proper replacements to this inhibitor are, and have been, studied worldwide. Special recent interest goes to rare earth metals [8–12] and Li salts [13–16], whether or not in combination with organic compounds, and Al-rich primers [17–20].

In the quest for potential Cr(VI) replacements, it is important to realize that critical steps in the inhibition process can be time-dependent [21]. Proper interpretation of these steps requires the use of analysis techniques that can investigate the inhibition process in real-time, under immersion (i.e. in-situ) and in a non-intrusive way. Many analysis techniques are however performed ex-situ, allowing an exact chemical or morphological analysis of the end state of the specimen under investigation, while lacking information of the time-dependence or kinetics of the process [5,6,22]. These experimental studies have proven to be highly valuable in the understanding of the complex corrosion mechanism of AA2024-T3 [5,6,22]. Ex-situ analysis of the metal surface after different exposure times can partially compensate for the lack of information on time-dependence in such cases [5,6]. A different criterion is whether or not an analysis technique is intrusive. Although to a limited extent, most electrochemical techniques able to provide direct information of the electrochemistry are in fact mildly intrusive; often a potential has to be applied to the system under investigation. An example is electrochemical impedance spectroscopy. Here, a small AC potential is applied to the system under investigation and the frequency resolved current response is in turn measured [23,24]. However, it should be noted that recent developments in this field make this technique increasingly interesting for the investigation of nonstationary corrosion behavior and inhibition, although at a cost of complexity increase [25,26].

The present work uses time-frequency information from electrochemical potential noise (EPN) data obtained with electrochemical noise (EN) measurements and in-situ optics to study corrosion

---

* Corresponding author.
E-mail address: AM.Homborg@mindef.nl (A.M. Homborg).

https://doi.org/10.1016/j.electacta.2021.139619
0013-4686/

and inhibition phenomena. The combination of time-frequency analysis of EPN with in-situ optical analysis was presented in earlier work, focusing primarily on the understanding of the different stages of the corrosion of AA2024-T3 [27]. The corrosion and inhibition processes are in this case not influenced by the measurement since both techniques are non-intrusive. The analysis of EPN data in the time-frequency domain provides kinetic information about the corrosion process [28,29]. Ever since Hladky and Dawson published their studies on potential fluctuations that were generated by localized corrosion [30,31], EN has been of particular interest to corrosion researchers. This can partly be explained by the attractive non-intrusive nature of the measurement, and partly by the ever increasing potential of signal analysis techniques [32]. Out of all these possibilities, time-frequency analysis is of particular interest, since it allows a direct, continuous investigation of (the evolution of) electrochemical process kinetics over time, without preconditions like e.g. stationarity or linearity, or the use of statistics [32]. Essentially, this analysis focusses on the time-frequency decomposition of transients in the EPN signal, features that Hagyard in his pioneering work in 1961 already recommended to study more closely, in order to better understand corrosion of aluminum [33].

The optical technique visualizes and quantifies macroscopic optical changes at the electrode surface, in-situ (during immersion) and with high spatiotemporal resolution. The technique uses iterative image analysis through ImageJ software [27,34]. The hyphenation of both techniques appears as a valuable combination for the study under immersion of corrosion and corrosion inhibition. The kinetic information from the time-frequency EPN analysis complements the optical analysis through the so-called activity maps. In this case, the combined optical-electrochemical analysis can reveal specific properties of inhibiting action, or the lack thereof.

In this work we focus on the study of the corrosion inhibition properties of two inhibitors ($Ce(NO_3)_3$, further denoted as Ce(III), and phytic acid, further denoted as PHA) on AA2024-T3 through the use of time-frequency analysis of EPN signals supported by activation maps obtained from in-situ optics. A largely neglected aspect of inhibiting layers is their stability after re-immersion in the absence of more inhibitor, to ensure long lasting protection. For this reason we additionally study the re-immersion properties after immersion in each inhibitor.

2. Experimental

A 2 mm thick rolled sheet commercial grade AA2024-T3 was supplied by Kaiser Aluminium and used as working electrode in all experiments. The sheets were milled and manually grinded to working electrode dimensions of 0.37±0.03 mm x 0.43±0.06 mm. Electrical contact was established with gold sputtering at the backside of the working electrode and the application of Cu adhesive tape. The working electrodes were embedded in an epoxy resin. The electrolytes used were aqueous NaCl solutions at a concentration of 0.05 M, made from demineralized water and analytical grade reagent. Depending on the type of experiment, these solutions additionally contain 1 mM $Ce(NO_3)_3$ or phytic acid (PHA). The ambient temperature was constant at 20 °C. The measurements involving Ce(III) were performed in triplicate, the immersion in PHA in duplicate and its re-immersion once, due to its indisputable lack of inhibition. The experimental setup was largely comparable to the one described in earlier work [27]. In the present work, the working electrode was mounted in a magnetic mount Raman electrochemical flow cell from Redox.me. This device allowed a total electrolyte volume of 4.5 ml and the use of a small Ag/AgCl (3 M KCl) reference electrode, also from Redox.me. The electrolyte was kept stagnant during all measurements. The entire experimental setup was placed inside a Faraday cage to avoid any electromagnetic disturbances and mounted on an optical table from ThorLabs. Fig. 1 shows an overview of the setup. The digital microscope, used for the optical analysis, is visible at the right-hand side of the setup. The electrochemical cell containing the working electrode, reference electrode and stagnant electrolyte was mounted on top of a (electrically) movable stage, visible at the left-hand side of the figures. This stage allowed movements in multiple directions in order to center and focus the working electrode for the microscope. This was only performed once prior to the start of each measurement, in order not to disturb the process during the experiments. The Faraday cage is visible as orange background at the backside in Fig. 1a.

The EN measurements were conducted in a 2-electrode configuration: the working electrode was connected to the reference electrode through a Compactstat from Ivium Technologies, working as potentiometer. The potentiometer was connected to a Windows-based PC running dedicated software. The sampling frequency was 20 Hz. A low-pass filter of 10 Hz was applied during data recording, in order to avoid aliasing. The maximum range of the potentiometer was set at 1 V, with a 24 bit resolution. The instrumental noise generated by this type of instrument was verified earlier through the procedure as described by Ritter et al. [35]. The EPN data were processed using Matlab from MathWorks. This analysis was based on the time-resolved energy distribution over frequency of the EPN signals, also denoted as the time-frequency domain. This is visualized in spectra produced by the continuous wavelet transform (CWT). CWT spectra extract localized frequency information, which can indicate the difference between for instance general or localized corrosion, or between different forms of localized corrosion [36]. Moreover, in the case of changing process kinetics over time, e.g. in the case of inhibition, CWT spectra visualize this by changes in the frequency characteristics of an EN signal over time [36]. Analogous to [36], the analytic Morlet wavelet was applied, as well as symmetric padding, or extension of the signal to avoid artefacts at the beginning and end of the CWT spectra. A window size with a duration of each time 5 ks serves to standardize the frequency range of the CWT spectra in this work, i.e. to keep the lowest frequency constant. Where applicable, transients in the EPN signals were located using an automated transient analysis technique based on modulus maxima in the CWT spectrum, which was published in earlier work [37]. Modulus maxima effectively indicate the locations of ridges, and therefore singularities or transients, in CWT spectra [37].

The optical analysis provided both qualitative and quantitative information about macroscopic surface changes with the use of iterative image analysis in ImageJ software. This analysis was similar to the one described in detail in earlier work by Denissen et al. [27]. The technique is based on a pixel-by pixel investigation of the progression of surface changes over time. The first image is used as a reference for all subsequent images. Lightening or darkening of each pixel with respect to that particular pixel at $t = 0$ is interpreted as an increase in intensity (or activity). Image conversion to a gray-scale at an 8-bit resolution allows the definition of 256 different levels of intensity between black and white. High-intensity pixels are isolated from low-intensity pixels in order to discriminate between active surface activity and background noise. In this way, the change in affected surface area, or so-called activity, can be calculated [27]. The overlap of the images with the SEM/EDS micrographs allows the classification of surface activity related to intermetallics. These SEM/EDS micrographs provided the composition and location of the intermetallic particles in the working electrode. Analogous to [38], The SEM (JEOL JSM-7500F field emission scanning electron microscope coupled with energy dispersive X-ray spectroscopy) was used in back-scattered electrons (BSE) mode. The accelerating voltage was 15 kV and the emission current 10 μA.

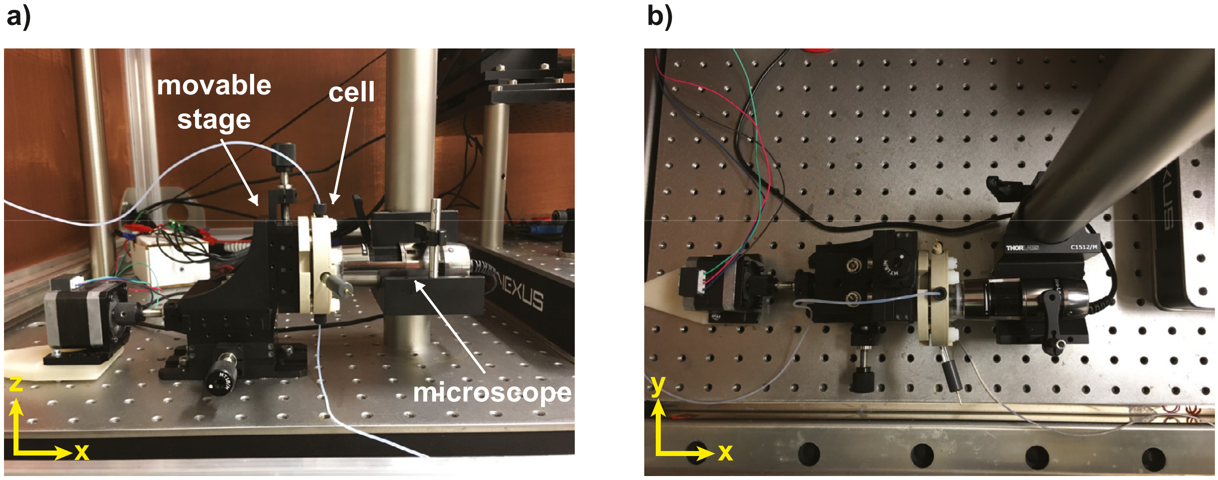

Fig. 1. (a) Front view and (b) Top view of the experimental setup.

3. Results and discussion

This section discusses the results of the in-situ optical and electrochemical analysis of Ce(III) and PHA, based on their corrosion inhibitive properties on AA2024-T3. Each inhibitor is investigated first based on the initial immersion in 0.05 M NaCl with the addition of the inhibitive species. After this, the stability of each inhibitor is investigated through re-immersion in 0.05 M NaCl. The standard corrosion characteristics of a AA2024-T3 micro-electrode immersed in 4.5 ml 0.05 M NaCl without inhibitor serve as a negative reference for both cases.

3.1. Reference system without inhibitor

Figs. 2a and b show the raw EPN signal between t = 0–2 ks (a) and 2–11 ks (b) of a AA2024-T3 micro-electrode immersed in 4.5 ml 0.05 M NaCl without inhibitor, together with the change in affected area over time calculated from the optical data. In order to investigate the kinetics of this reference corrosion process and to compare this with those in the presence of the inhibitors in the solution, Fig. 2c shows a CWT spectrum of the EPN signal from t = 2–7 ks. As a visual aid, the original EPN signal is projected with its relative amplitudes in the X-Z plane at the backside of the spectrum, in order to facilitate correct interpretation of the time-frequency information and to correlate it to transients in the raw data. The amplitude scale indicated along the z-axis corresponds to the amplitudes of the CWT spectrum, indicated in the color bar at the right hand side of the figure.

After the measurement, approximately 30% of the surface area is affected due to the corrosion process, as visible in Fig. 2b. The CWT spectrum in Fig. 2c shows an almost continuous range of amplitudes below 10^{-2} Hz, with a clear maximum between 2 and 2,5 ks. This essentially means that a relatively large part of the energy in the EPN signal is concentrated at low frequencies, which is usually observed for processes that are predominantly under diffusion control, or in other words: in the case of advanced localized corrosion associated with stable pit growth [39]. A significant contribution of transients is visible in the high-frequency range, e.g. at t = 3,3 ks between $5 \bullet 10^{-2}$ – 10 Hz. Earlier work investigating time-frequency characteristics of EN data of larger AA2024-T3 electrodes (working electrode area 5 mm^2) in bulk NaCl solution showed these features to a smaller extent [40]. Therefore, this difference is probably caused by either: 1) a different cathode – anode ratio due to the smaller working electrode area, or 2) a different ratio between the electrolyte volume and working electrode area. The exact reason is unclear to the authors and will be subject of study in future works.

3.2. Corrosion inhibition

3.2.1. Cerium(III)

The first inhibitor studied with the combined electrochemical and optical technique is $Ce(NO_3)_3$. Fig. 3a shows the raw EPN data signal, as well as the change in affected area, of a AA2024-T3 micro-electrode immersed in 0.05 M NaCl with 1 mM $Ce(NO_3)_3$. Figs. 3b-d show the microstructure of the electrode after overlapping the result of dedicated SEM-EDS analysis to locate the intermetallics (intermetallics marked in yellow) on the optical images obtained during immersion. Figs. 3e-g show the activity maps at three different immersion time instants, calculated from the space-time-resolved optical images (darker colors indicate more activity). The time instants reflect the microstructure at the start, at the onset of the OCP increase and at the start of the region where the OCP stabilizes. Figs. 3h-j show the CWT spectra related to these optical results, from t = 6–11 ks (h), from t = 27–32 ks (i) and from t = 32–37 ks (j).

The process can be divided into three different stages, numbered I-III in Fig. 3a. In stage I, the OCP decreases to reach a minimum potential value, i.e. the overall surface potential becomes less noble, in agreement with previous reports assigning a cathodic inhibiting nature to Ce^{3+} (i.e. its presence makes cathodic sites less cathodic and the overall surface more anodic). The raw EPN data in this stage is relatively smooth and dominated by a DC drift. At the end of this stage, small transients appear in the OCP signal. After 11 ks, in stage II the OCP increases again according to Fig. 3a. Additionally, optical activity starts in this stage. This is also visible in the similarity between Figs. 3b and e with Figs. 3c and f, indicating no surface changes at t = 11 ks. The activity that starts after 11 ks is localized at the intermetallics; the matrix is still unaffected at t = 32 ks, as seen in Figs. 3d and g. The detected activity at the intermetallics is preceded with high-frequency activity in the CWT spectrum of Fig. 3h, where local maxima above $3 \bullet 10^{-1}$ Hz are dominant. Unfortunately, the optical setup and approach was unable to identify the locations where the inhibitor acts in this first immersion phase. Given the differences between this CWT spectrum and that of AA2024-T3 in 0.05 M NaCl in Fig. 2c, the onset of inhibitor activity is probably not detected optically in this case, only with the electrochemical technique. This indicates that changes occur at a molecular level, i.e. below the optical resolution.

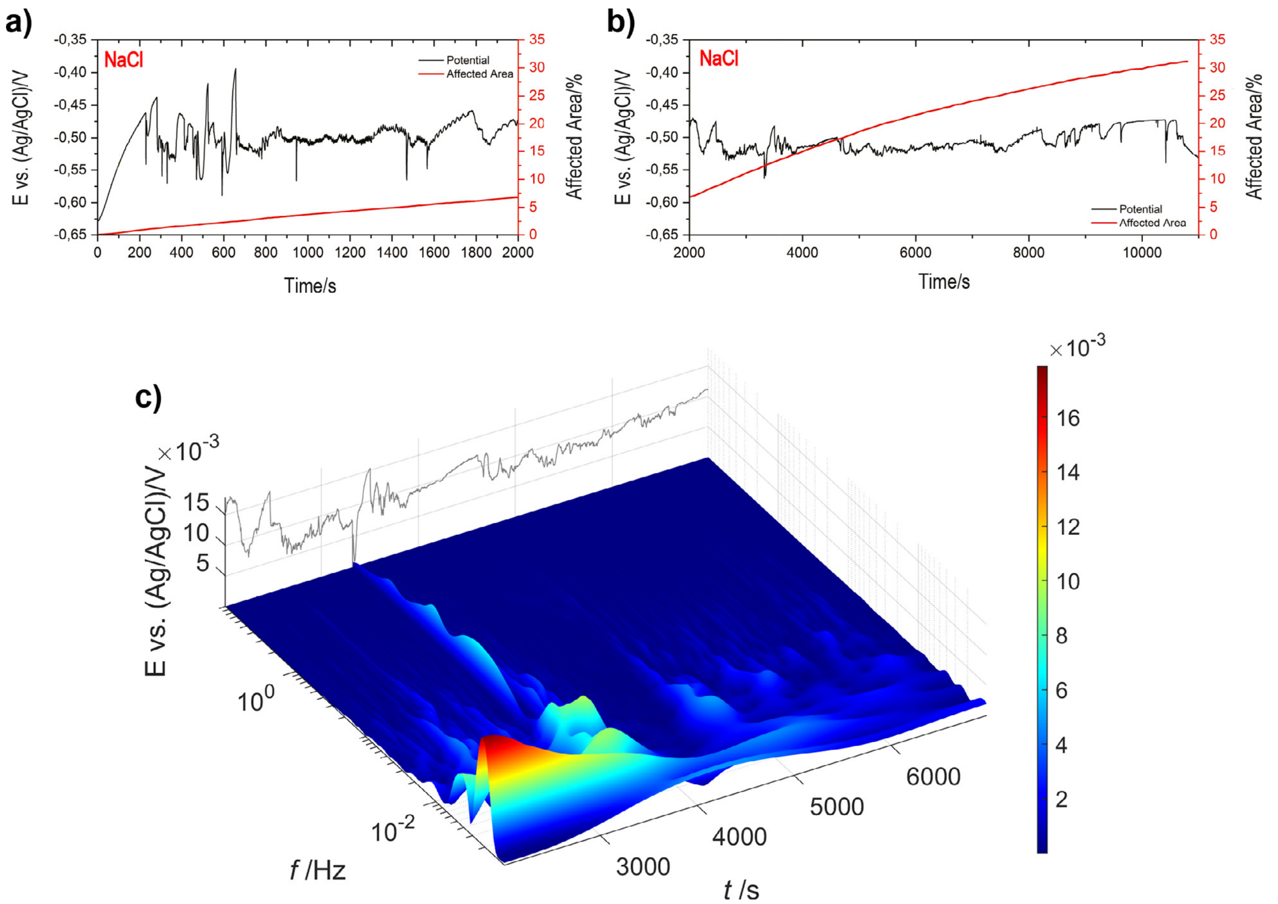

Fig. 2. Raw EPN signal with change in affected area, from $t = 0$–2 ks (a) and 2–11 ks (b) of a AA2024 T3 micro-electrode immersed in 4.5 ml 0.05 M NaCl without inhibitor. Fig. 2c CWT spectrum from $t = 2$–7 ks.

Stage III starts at 32 ks, Figs. 3d and g show a clear activity increase at the intermetallics, which started already after 11 ks, given the increase of affected area from that instant in Fig. 3a. The CWT spectra of Figs. 3i and j, together with the increase in transient amplitudes that is visible in Fig. 3a, further classify this activity. The activity increase at the intermetallics around $t = 32$ ks marks a transition in electrochemistry kinetics. In Fig. 3i, from 27 to 32 ks the kinetics are still similar to those between 6 and 11 ks, which was related to inhibitor activity. This changes towards a type with frequencies below 10^{-2} Hz dominating the CWT spectrum between 32 and 37 ks in Fig. 3j. Combined with the absence of significant further increase of affected area in Fig. 3a, this indicates the dominance of slow phenomena related in this case to slow (Ce-hydr-) oxide build-up at/around the intermetallics, and the likely change in oxide type from 3-valent Ce ($Ce(OH)_3$) to 4-valent Ce (less soluble $Ce(OH)_4$ or CeO_2) [41–43]. The first protective layer formed limits further oxide build-up. This is also in agreement with the relatively stable OCP in this third stage, suggesting no further change in surface composition. It should be noted that duplicate measurements did not show the first decrease in OCP, together with the accompanying onset of high-frequency transients. Instead, these samples exhibited a typical corrosion signal at an earlier stage. One possibility for this difference is the hypothesis that the deposition of (Ce-hydr-) oxide requires a limited initial corrosion activity, generating an increased local pH [41,42]. In the measurement presented in this work, this initial corrosion activity is very limited, since surface activity remained below the detection threshold of the optical analysis until 11 ks (Fig. 3a). Moreover, Fig. 3h shows only dominant inhibitor activity in this first stage. For this work it is important that the integrated electrochemical and optical technique identifies inhibitor activity, as well as a possible eventual loss of inhibition.

3.2.2. PHA

The second inhibitor studied with the combined electrochemical and optical technique is PHA. Fig. 4a shows the raw EPN data signal with the change in affected area of a AA2024-T3 microelectrode immersed in 0.05 M NaCl with 1 mM PHA. Figs. 4b and c show the microstructure of the electrode before and after exposure (intermetallics marked in yellow). Figs. 4d and e show the associated activity maps (darker colors indicate more activity). Figs. 4f-h show CWT spectra from 0 to 5 ks (f), 10–15 ks (g) and 15–20 ks (h).

The raw data signal shown in Fig. 4a indicates that the OCP initially increases steeply from $t = 0$–1 ks, followed by a much more gradual increase with transient amplitudes sometimes exceeding 300 mV until approximately 11,5 ks. Subsequently, it decreases towards −0.65 V vs Ag/AgCl, with diminishing transient amplitudes. The surface area remains largely unaffected over the course of the measurement. A limited localized change of affected surface area is visible after approximately $t = 17$ ks, towards approximately 1,5% after the entire measurement. This is further acknowledged by the micrographs shown in Figs. 4b-e: only a limited change of the surface is visible in Figs. 4c and e with respect to the surface before exposure, as shown in Figs. 4b and d. Moreover, the surface changes occur more at the edges of the working electrode, as well as around a small number of intermetallics. This a marked difference with Ce(III), where the surface changes occurred predominantly at the locations of the intermetallics. The initial steep OCP increase indicates that the PHA acts like an anodic inhibitor, and

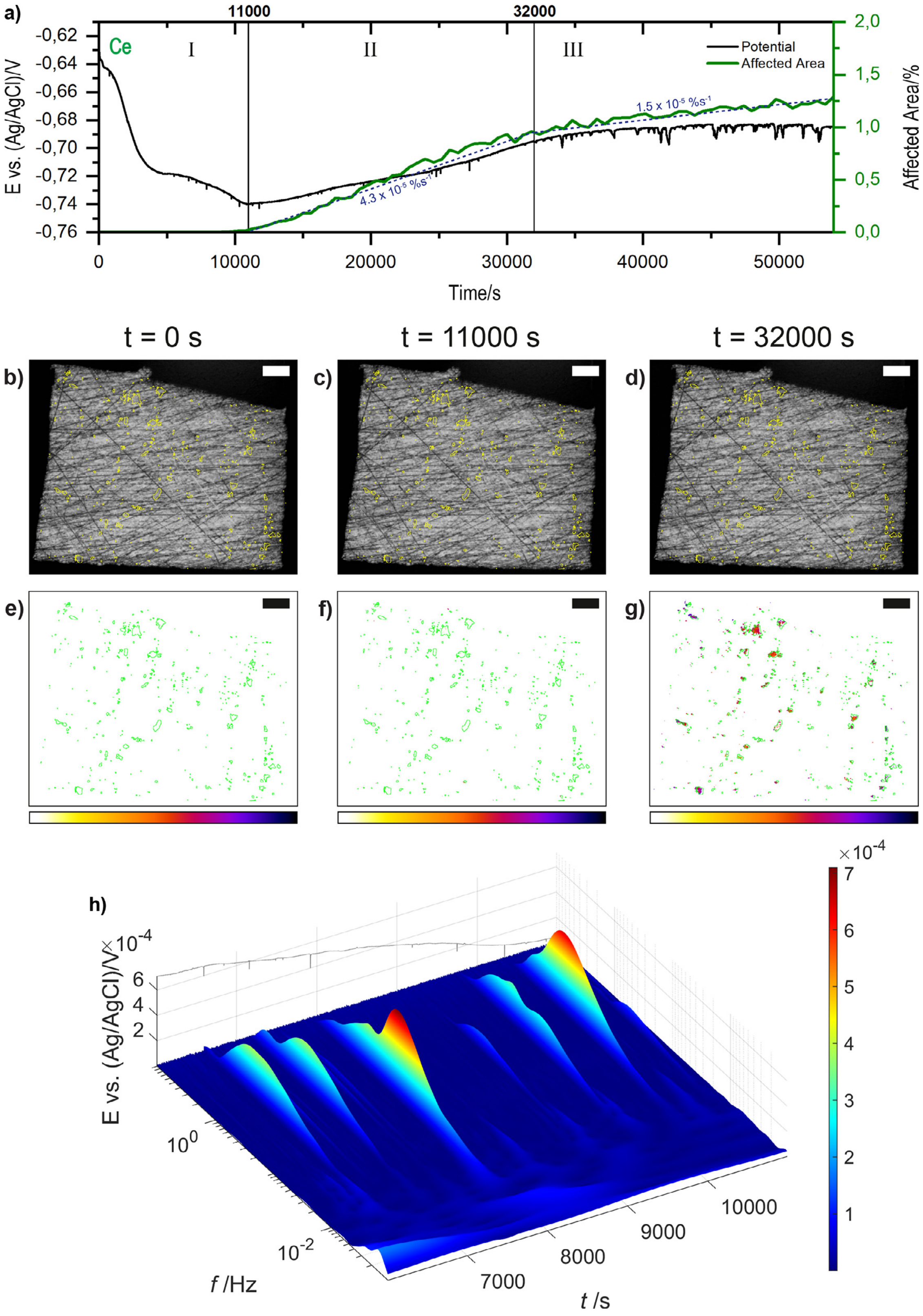

Fig. 3. (a) Raw EPN data with the change in affected area of a AA2024-T3 micro-electrode immersed in 4.5 ml 0.05 M NaCl with 1 mM Ce(NO$_3$)$_3$, (b-d) Microstructure (intermetallics in yellow) at t = 0 (b), after 11 ks (c) and 32 ks (d), (e-g) Activity maps (in color scale, intermetallics in green) at the same time instants, (h-j) CWT spectra related to these optical results, from t = 6–11 ks (h), from t = 27–32 ks (i) and from t = 32–37 ks (j).

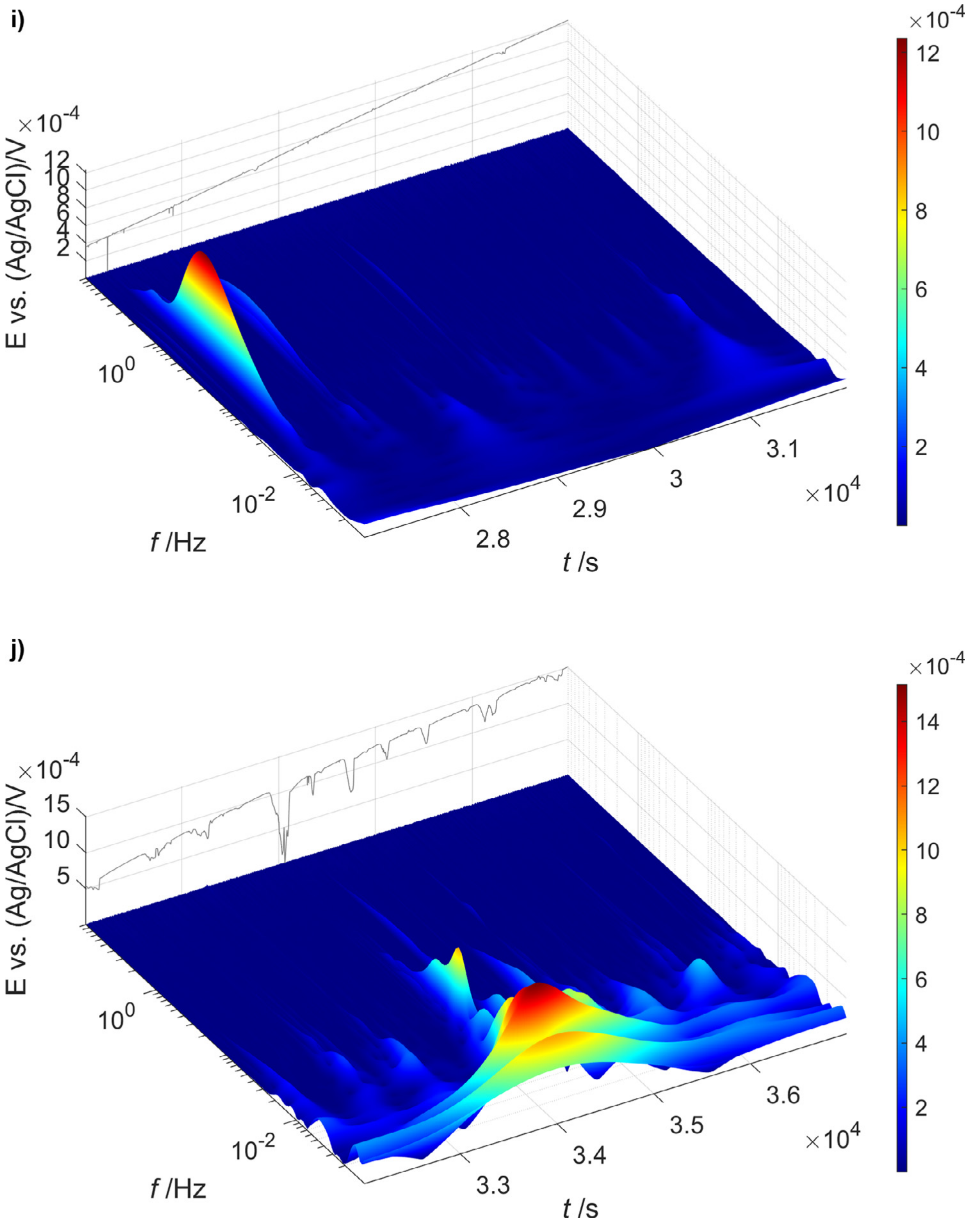

Fig. 3. Continued

the limited total affected area in Fig. 4a combined with the limited number of coloured spots in Fig. 4e as compared to Fig. 4d indicates that indeed no notable corrosion has taken place. In order to better understand the kinetics of the process indicated by the CWT spectra shown in Figs. 4f-h, Fig. 5 shows the associated raw EPN data signal with the transient locations indicated with gray vertical lines.

Figs. 4f and g show that from 0 to 11,5 ks the energy distribution in the CWT spectrum is notably different than that of the reference corrosion process of AA2024-T3 in 0.05 M NaCl. Local maxima exist between 10^{-2} – 10^{-1} Hz instead of at/under 10^{-2} Hz. In addition, in between the transients, the EPN signal is smooth. This results in relatively isolated groups of transients, indicated by Figs. 5a and b. Subsequently, the OCP decrease that was visible in Fig. 4a at approximately 11,5 ks marks a significant transition in process kinetics in terms of energy distribution as well as transient density over time. From this time instant, Fig. 4g shows that the energy distribution gravitates more towards the frequency range below 10^{-2} Hz. This still differs from the frequency decomposition of the corrosion of AA2024-T3 in 0.05 M NaCl, in that the relative contribution of frequencies in the range of 10^{-2} Hz to 10^{-1} Hz is considerably larger. In addition, the amplitudes of the CWT spectrum are over 4x larger as compared to those in Fig. 2c. Fig. 5b indicates a clear increase in transient density over time at $t = 11{,}5$ ks. Finally, the change of affected surface area that is visible in Fig. 4a after approximately $t = 17$ ks is accompanied by a strong reduction in overall energy and local maxima below 10^{-2} Hz, shown in Fig. 4h. Fig. 5c indicates that the transient density over time also decreases again in this time window. Hence, the electrochemistry changes towards a lower intensity, more diffusion-controlled signature. Due to the final steady-state of the OCP and the absence of transients in this last stage the measurement is shorter as compared to the measurement on Ce(III).

It can be discussed that the combined electrochemical and optical procedure describe the process as:

1) From $t = 0$–11,5 ks: PHA inhibits anodic sites, inducing the initial OCP increase and lack of affected area (Fig. 4a), generat-

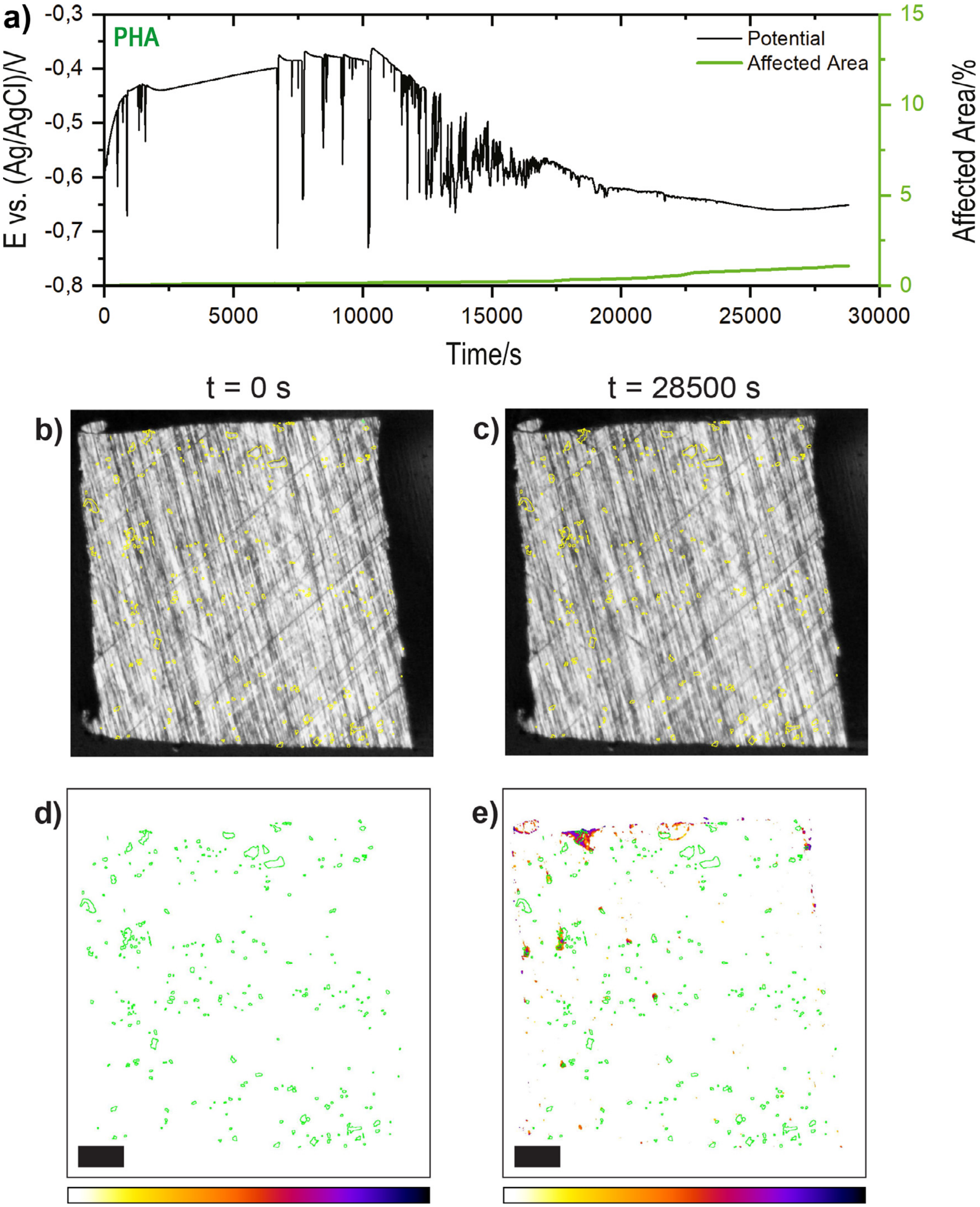

Fig. 4. (a) Raw EPN signal with the change in affected area of a AA2024-T3 micro-electrode immersed in 4.5 ml 0.05 M NaCl with 1 mM PHA, (b-c) Microstructure before and after exposure (intermetallics in yellow), (d-e) Activity maps (in color scale, intermetallics in green) at the same time instants, (f-h) CWT spectra from 0 to 5 ks (f), 10–15 ks (g) and 15–20 ks (h).

ing the typical energy distribution (Figs. 4f and g) and isolated transients (Figs. 5a-b). The optical technique is unable to detect this inhibitor activity in this case, as it occurs on a molecular level;

2) From $t = 11{,}5$–17 ks: Gradual breakdown of the protective film. Interaction between PHA and the electrode surface that marks the transition from inhibitor activity to limited corrosion activity. This is accompanied by the absence of affected surface area and a decreasing OCP (Fig. 4a), marked changes in energy distribution (Fig. 4h) and an increasing transient density (Fig. 5c);
3) From 17 ks, limited corrosion activity. This is indicated by a small increase in affected surface area and a stabilization of the OCP level (Figs. 4a-e), a strong reduction in overall energy and changes in energy distribution (Fig. 4h) and decreasing transient density (Fig. 5c).

Comparing the electrochemical and optical results for both inhibitors, their respective cathodic and anodic nature is clearly visible in the data. Despite their differences in OCP behavior, in both cases the optical technique requires some time for the surface activity to become visible. At the end of each measurement, only a limited total surface area is affected, in the order of 1–2%. For both inhibitors it is also clear that the surface activity occurs highly localized: at (Ce(III)) or near (PHA) the locations of the inter-

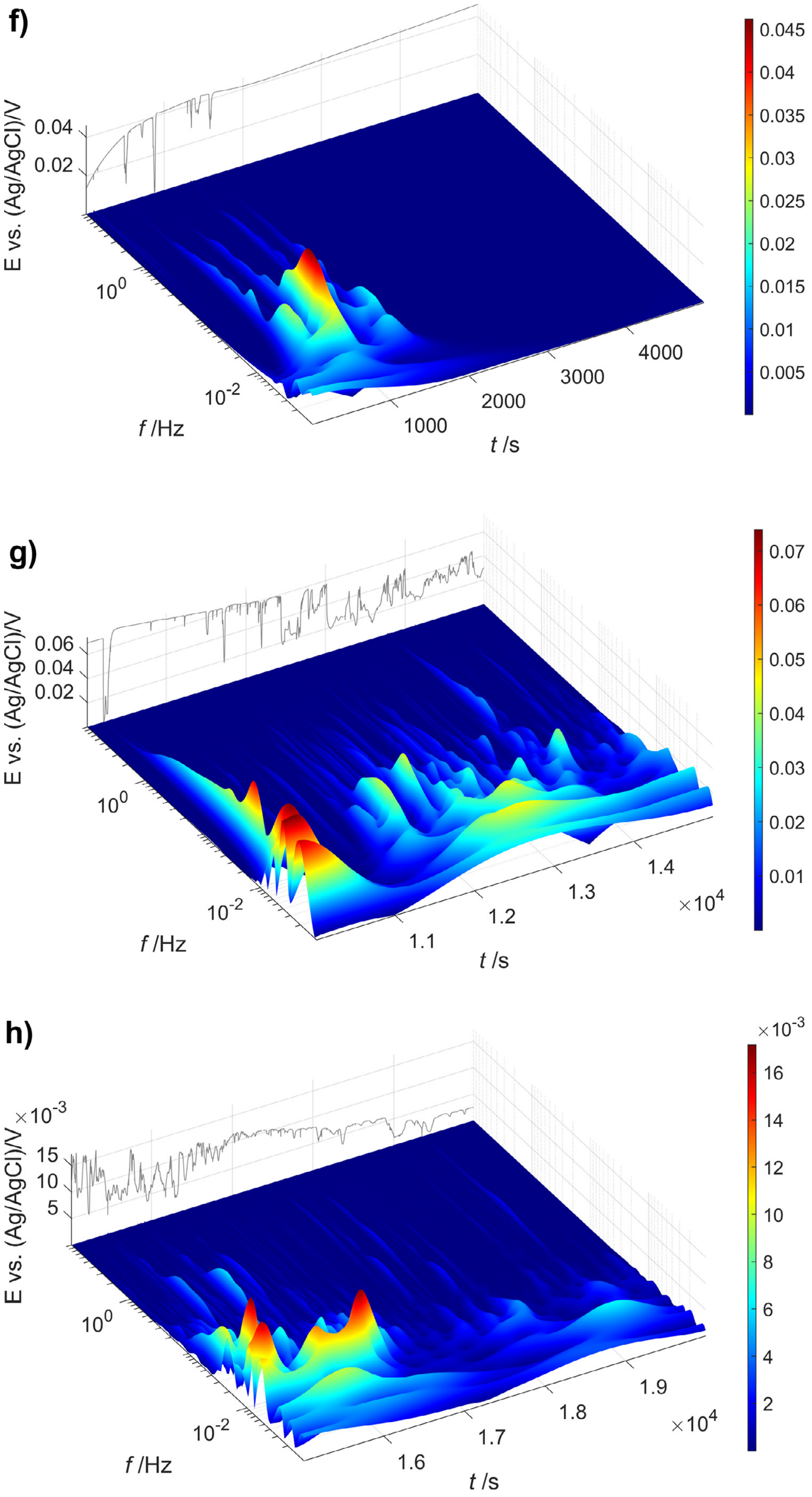

Fig. 4. Continued

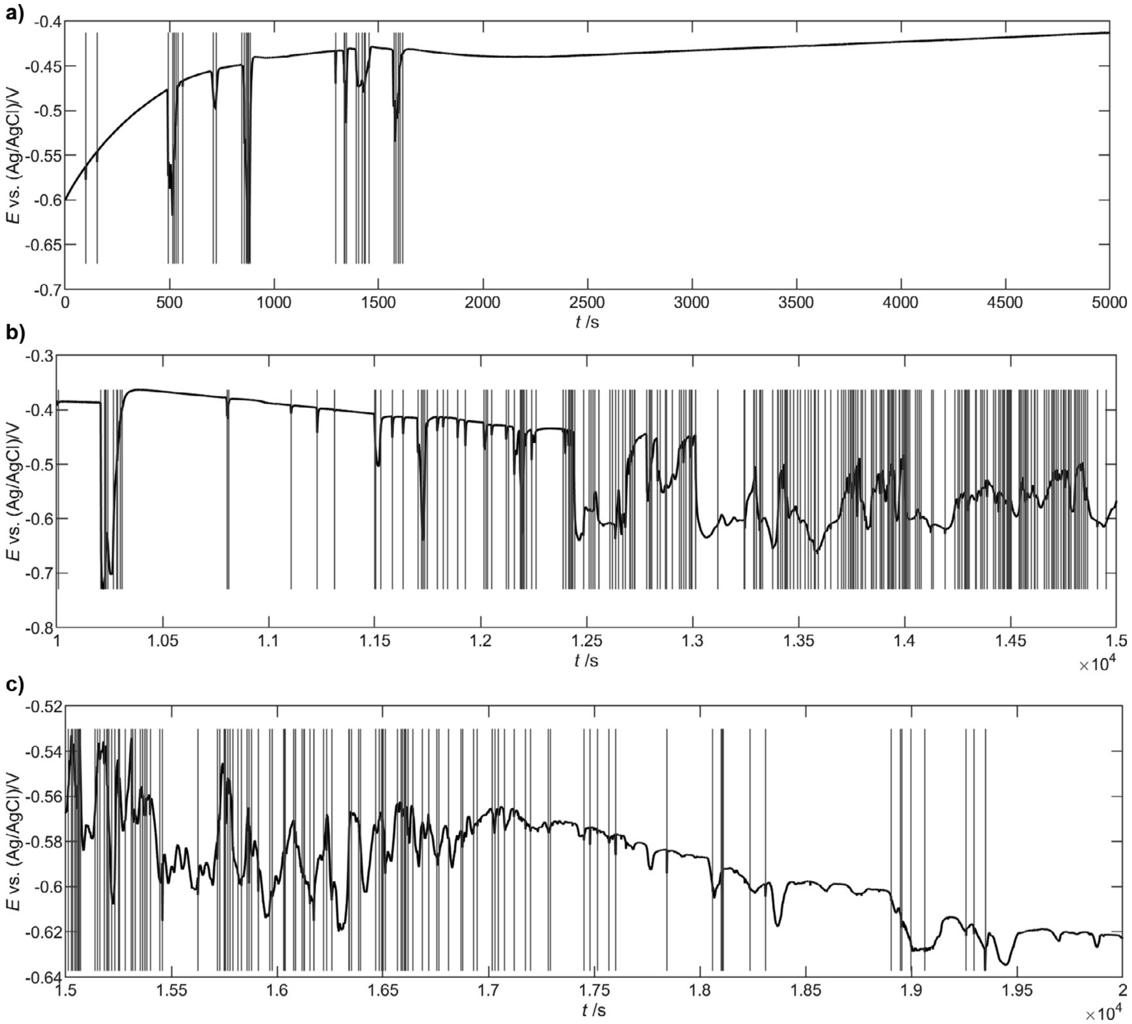

Fig. 5. Raw EPN signal with transient locations indicated by gray vertical lines from 0 to 5 ks (a), 10–15 ks (b) and 15–20 ks (c) of a AA2024-T3 micro-electrode immersed in 4.5 ml 0.05 M NaCl with 1 mM PHA.

metallics. In the case of Ce(III), this fast, localized activity initially generates small, high-frequency potential transients, in the order of a few mV. For PHA, the transients are much larger, sometimes exceeding 300 mV. Their dominant frequencies are approximately a decade lower than compared to Ce(III) activity. Still, both types of inhibition and interaction between inhibitor and electrode surface can be distinguished from the reference corrosion activity of AA2024-T3. PHA allows limited corrosion after approximately 17 ks, whereas in the case of Ce(III) slow (Ce-hydr-) oxide build-up takes place at/around the intermetallics after 32 ks. In the latter case, the first protective layer formed probably limits further oxide build-up.

3.3. Re-immersion

In order to further verify the stability of the inhibitive layer, the samples are re-immersed in 0.05 M NaCl after their initial exposure in electrolyte containing 1 mM $Ce(NO_3)_3$ or 1 mM PHA.

3.3.1. Cerium(III)

Fig. 6a shows the raw EPN data of the re-immersion measurement for $Ce(NO_3)_3$, together with the change in activity area. Figs. 6b-d show the microstructure of the electrode (intermetallics marked in yellow). Figs. 6e-g show the activity maps at three different immersion time instants (darker colors indicate more activity). The time instants reflect the microstructure at the start, at the onset of the increase in affected area and at the end of the re-immersion. Fig. 6h shows the CWT spectrum from t = 0,2–5,2 ks.

Fig. 6a shows that right after immersion the OCP gradually increases towards more noble values and a steady-state after around 12 ks immersion. Small optical variations are observed in the first 1.8 ks, followed by clear activity increase as indicated by the green vertical transition mark. In addition, the transient amplitude decreases. The first 200 s of the EPN signal exhibits significant upwards drift. The CWT spectrum of Fig. 6h is similar in energy distribution over frequencies to that of the reference corrosion process of AA2024-T3 in 0.05 M NaCl, which was shown in Fig. 2c. Hence, re-immersion immediately activates corrosion. After 3 ks only gradual, stable localized AA2024-T3 corrosion remains: the energy above $2{\bullet}10^{-2}$ Hz disappears almost entirely. The optical analysis in Fig. 6a shows a limited affected area in this case: slightly more than 6% after 5 h of immersion, as compared to over 30% in the reference case of AA2024-T3 corrosion without initial inhibition (Fig. 2a).

Figs. 6c and f, as compared to Figs. 6b and e, show activity located around the intermetallics starting from t = 1,8 ks. From a mechanistic point of view, it is likely that Ce-oxide/hydroxide layers undergo a progressive re-dissolution combined with Cl attack, causing the typical fast transients in Fig. 6h. The cracked structure of the Ce-containing layer could facilitate this re-dissolution [44]. Comparing Figs. 6d and g with Figs. 3d and g, the larger

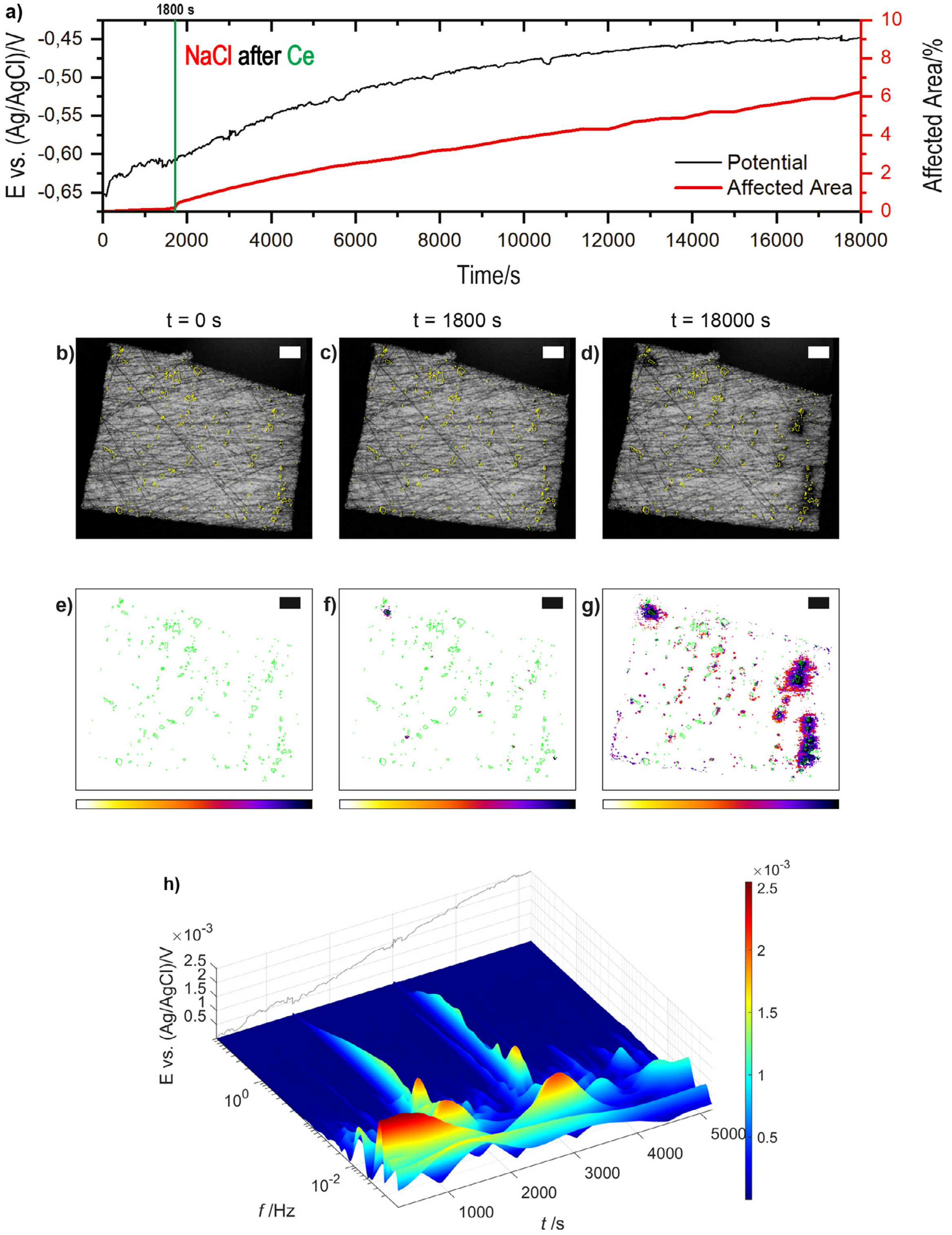

Fig. 6. (a) Raw EPN data with the change in affected area of a AA2024-T3 micro-electrode immersed in 4.5 ml 0.05 M NaCl, after an initial exposure to 0.05 M NaCl with 1 mM $Ce(NO_3)_3$, (b-d) Microstructure (intermetallics in yellow) at $t = 0$ (b), after 1,8 ks (c) and 18 ks (d), (e-g) Activity maps (in color scale, intermetallics in green) at the same time instants, (h) CWT spectrum from $t = 0{,}2–5{,}2$ ks.

areas around the locations of the intermetallics, where no Ce-oxide/hydroxide layers would be formed during the initial exposure to Ce(III) (Figs. 3d and g), indicate that also the Al matrix is affected in this case. The instability of the protective Ce-containing layer after re-immersion in NaCl solution was also demonstrated in earlier work [40], where after the initial 1 ks of re-immersion in NaCl the working electrode would be in a similar state as compared to corrosion of bare AA2024-T3 in 0.05 M NaCl. This instability causes gradual exposure of the underlying intermetallic particle, which in turn reactivates micro-galvanic effects. Ce-ions, like any inhibitor, are not considered to be able to inhibit processes occurring below the surface [45,46].

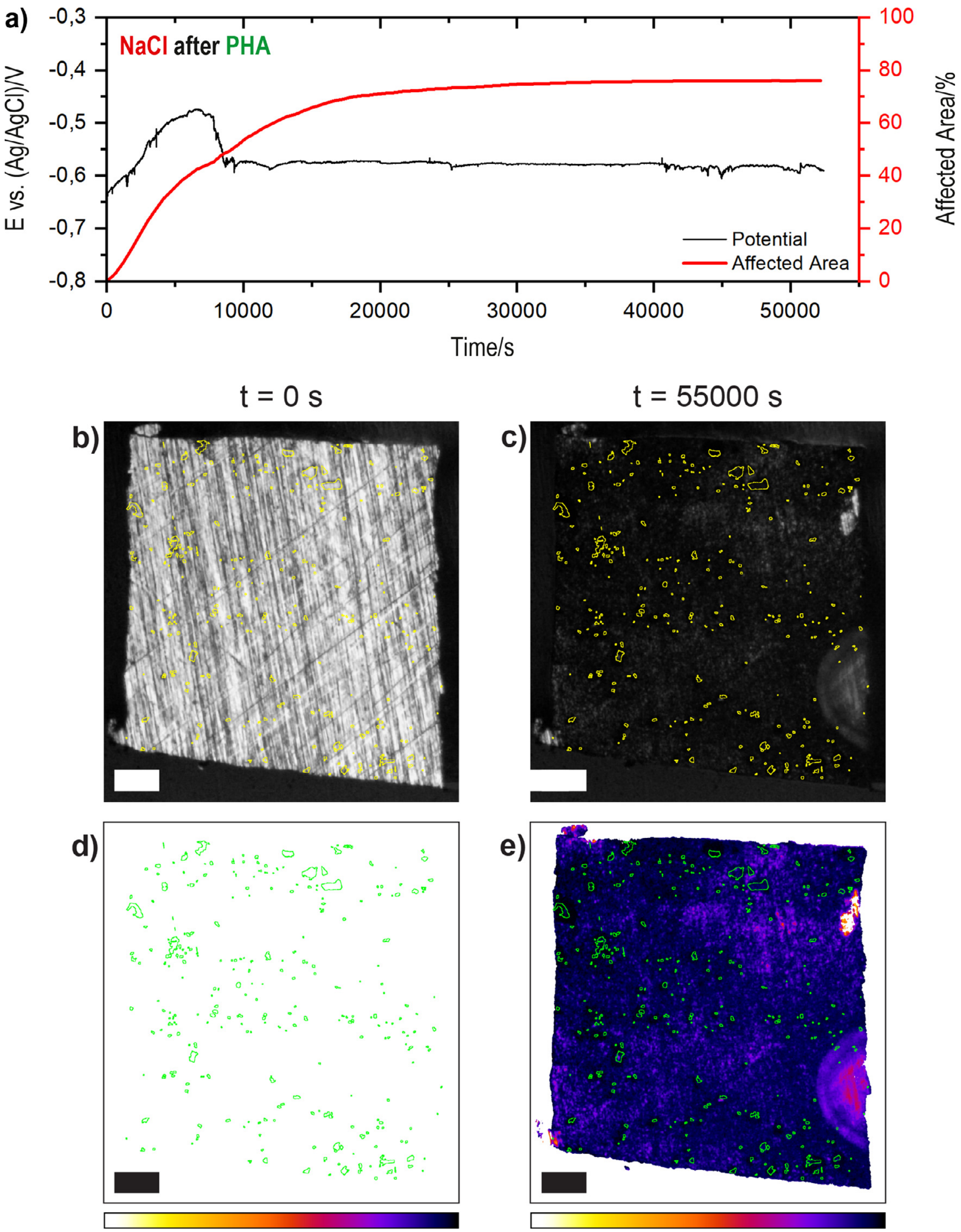

Fig. 7. (a) Raw EPN data with the change in affected area of a AA2024-T3 micro-electrode immersed in 4.5 ml 0.05 M NaCl, after an initial exposure to 4.5 ml 0.05 M NaCl with 1 mM PHA, (b-c) Microstructure before and after exposure (intermetallics in yellow), (d-e) Activity maps (in color scale, intermetallics in green) at the same time instants, (f-h) CWT spectra from t = 0–15 ks, separated in each time 5 ks.

3.3.2. PHA

Fig. 7a shows the raw EPN data of the re-immersion measurement for PHA, with the change in affected area. Figs. 7b and c show the microstructure of the electrode before and after exposure (intermetallics marked in yellow). Figs. 7d and e show the associated activity maps (darker colors indicate more activity). Figs. 7f-h show CWT spectra from t = 0–15 ks, separated in each time 5 ks.

Interestingly, in Fig. 7a, from t = 0–7,5 ks the EPN drifts upwards towards to −0.47 V vs Ag/AgCl, followed by a relatively fast drop towards a steady-state value of −0.58 V vs Ag/AgCl. The affected area increases with decreasing rate from t = 0–30 ks and remains more or less steady from t = 30 ks onwards. From t = 0–7,5 ks, the increasing OCP is accompanied by an increase of affected area of approximately 40%. A final affected area of approximately 75% indicates large changes at the electrode surface in the first 30 ks. This is further acknowledged by the micrographs: Figs. 7c and e (after exposure) with Figs. 7b and d (before exposure) show that the entire area is heavily affected after exposure. Moreover,

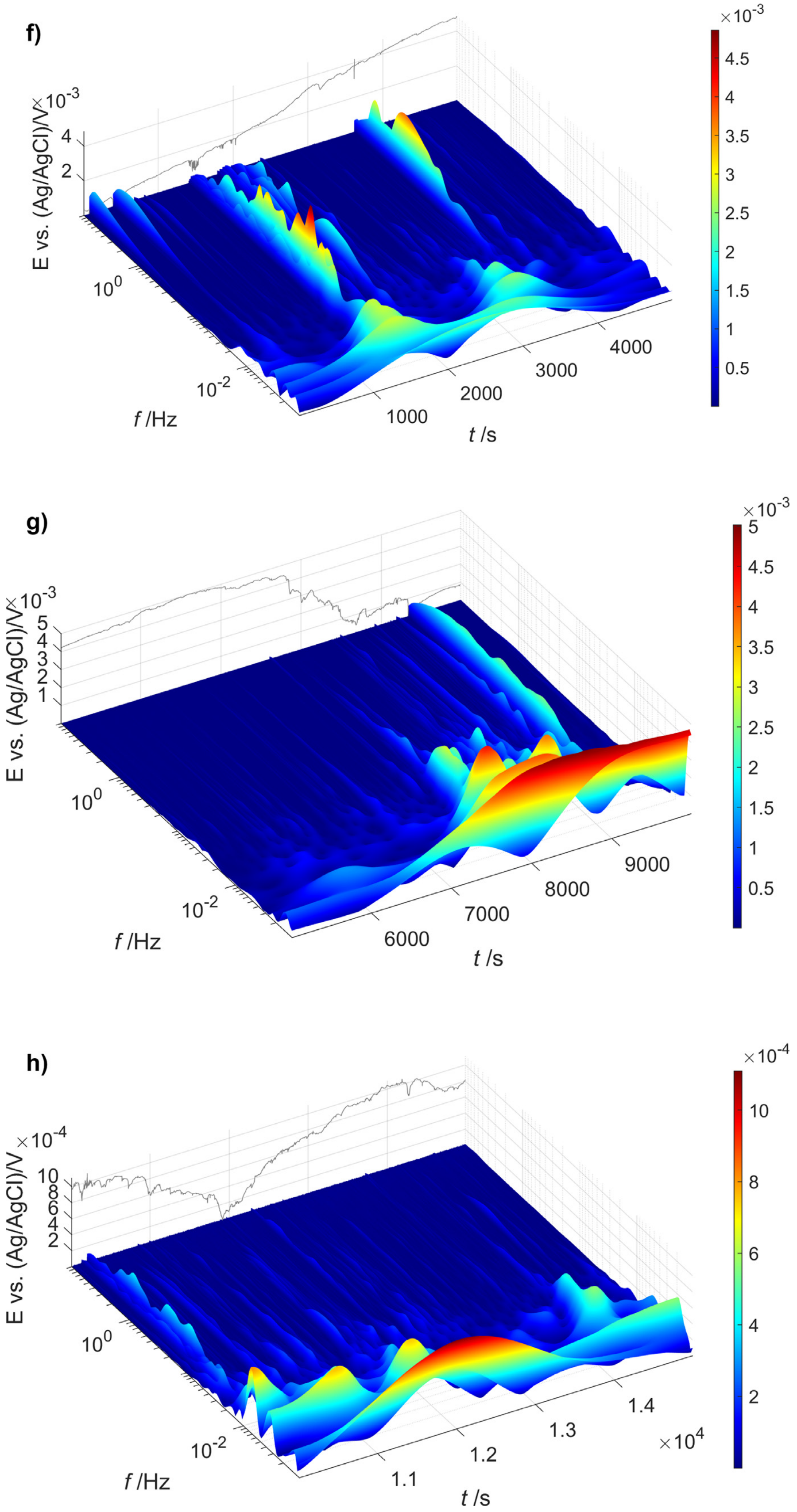

Fig. 7. Continued

the surface changes are generally spread over the surface and not limited to areas at/around the intermetallics in this case. After 10 ks already approximately 50% of the surface is affected, whereas in the case of the reference corrosion process of AA2024-T3 as presented in Fig. 2b, only 30% was affected after 10 ks. The process kinetics shown in the CWT spectrum in Fig. 7f indicate fast, high-energy transients with local maxima above 10^{-1} Hz. These are indicated by the dark gray arrow and are related to the desorption process. These transients occur alongside a significant extra low-frequency component below 10^{-2} Hz indicated by the light gray arrow, with comparable amplitudes, which are typical for AA2024-T3 corrosion. From 7,5–10 ks, the OCP drop is accompanied by an energy distribution in the CWT spectrum which is typical for AA2024-T3 corrosion, as shown in Fig. 7g. After reaching a steady OCP after 10 ks, the maximum amplitudes in the CWT spectrum of Fig. 7h are over a decade lower as compared to those of the CWT spectrum of Fig. 2c. However, the typical energy distribution associated with corrosion activity for this alloy remains. This agrees with the optical observation in Fig. 7a of a slower increase of affected surface as compared to t = 0–7,5 ks. The following mechanism is proposed:

1) From t = 0–7,5 ks: Desorption of PHA from the surface induces the OCP increase (Fig. 7a). This is combined with the onset of corrosion, causing a significant increase in affected area (Fig. 7a). Each of both processes produces part of the energy distribution in the CWT (Fig. 7f)
2) From t = 7,5–10 ks: Further activation of the surface (corrosion), after desorption of PHA is completed, generating an OCP decrease and further increase of affected area (Fig. 7a), as well as a CWT energy distribution typical for corrosion of AA2024-T3 (Fig. 7g);
3) Finally, limited corrosion progression, visible in the affected area after exposure (Figs. 7c and e), the relatively steady OCP and the decreasing rate of the increase of affected area (Fig. 7a), as well as a CWT energy distribution typical for corrosion of AA2024-T3, with notably lower amplitudes as compared to the reference corrosion process of this alloy (Fig. 7h).

Comparing the two inhibitors with regard to their protection after re-immersion in 0.05 M NaCl, it is obvious that the performance of Ce(III) exceeds that of PHA, although both inhibitors cannot effectively protect the substrate in this case. For Ce(III), the activity was concentrated mainly around the intermetallics (Figs. 6b-g), which gave rise to fast transients in the EPN (Fig. 6h). In the case of PHA, the attack was much more general (Figs. 7b-e), giving rise to a more diffusion-controlled time-frequency signature in the CWT (Fig. 7h). Although the total exposure time for the re-immersion after exposure to PHA was larger, Fig. 7a shows that even after 18 ks the total affected area already exceeded 70%, as compared to 6% for the re-immersion after exposure to Ce(III) (Fig. 6a).

4. Conclusion

The effectiveness and durability of cerium(III) (Ce(III)) and phytic acid (PHA) as corrosion inhibitor for AA2024-T3 could be discriminated well by the combination of time-resolved frequency analysis of electrochemical potential noise combined with the in-situ optical technique. Both Ce(III) and PHA were not capable to inhibit corrosion to a large extent, as re-immersion led to electrochemical (corrosion) activity for both inhibitors. In the presence of inhibitor in solution, the surface activity occurs highly localized: at (Ce(III)) or near (PHA) the locations of the intermetallics. In the case of re-immersion, for Ce(III) the Cl attack on deposited Ce-oxide/hydroxide layers, possibly combined with corrosion activity of the Al matrix, generates surface activity again around the intermetallics. However, for PHA the re-immersion affects the entire surface.

In a general sense, time-frequency analysis of electrochemical potential noise provides a direct insight in the (change in) kinetics of the electrochemical processes over time. This technique allows to distinguish between different types of corrosion and/or inhibitor activity, combined with changes in affected area provided by the in-situ optical technique. The latter in turn provides a direct view of associated changes in surface properties and morphology. Therefore, the in-situ optical technique allows to quantify electrochemical activity visible with electrochemistry. By combining both techniques, time-variant changes between corrosion, inhibitor activity, inhibited state and re-activation could effectively be discriminated from each other.

The present work focusses on the signal characteristics on a larger scale, and hence on the overall system kinetics. As a recommendation, transients could be investigated individually and correlated to local instantaneous surface changes, e.g. around precipitates. This will further increase the understanding of the interaction between inhibitor and substrate material, and contribute to effective corrosion inhibition in practical cases.

Credit authorship contribution statement

Axel Homborg: Writing, Software, Formal analysis, Investigation, Validation. **Matteo Olgiati**: Software, Formal analysis, Investigation, Validation. **Paul Denissen**: Conceptualization, Software, Formal analysis, Investigation, Validation. **Santiago Garcia**: Supervision, Conceptualization, Writing

Declaration of Competing Interest

The authors declare that they have no known competing financial interests or personal relationships that could have appeared to influence the work reported in this paper.

Acknowledgements

The authors would like to acknowledge the Faculty of Aerospace Engineering at Delft University of Technology and the Netherlands defence Academy for accommodating the research work.

References

[1] R.L. Twite, G.P. Bierwagen, Review of alternatives to chromate for corrosion protection of aluminum aerospace alloys, Prog. Org. Coat. 33 (1998) 91–100.
[2] A.E. Hughes, N. Birbilis, J.M.C. Mol, S.J. Garcia, X. Zhou, G.E. Thompson, High Strength Al-Alloys: Microstructure, Corrosion and Principles of Protection, in: Z. Ahmad (Ed.), Recent Trends Process. Degrad, Alum. Alloy., InTech,, 2011, pp. 223–262.
[3] N.L. Sukiman, X. Zhou, N. Birbilis, A.E. Hughes, J.M.C. Mol, S.J. Garcia, X. Zhou, G.E. Thompson, Durability and Corrosion of Aluminium and Its Alloys: Overview, Property Space, Techniques and Developments, in: Z. Ahmad (Ed.), Alum. Alloy. - New Trends Fabr. Appl., InTech, 2012: pp. 57–64. https://doi.org/10.5772/53752.
[4] R.G. Buchheit, R.P. Grant, P.F. Hlava, B. Mckenzie, G.L. Zender, Local Dissolution Phenomena Associated with S Phase (Al2CuMg) Particles in Aluminum Alloy 2024-T3, J. Electrochem. Soc. 144 (1997) 2621–2628.
[5] A. Boag, A.E. Hughes, A.M. Glenn, T.H. Muster, D. McCulloch, Corrosion of AA2024-T3 Part I: localised corrosion of isolated IM particles, Corros. Sci. 53 (2011) 17–26, doi:10.1016/j.corsci.2010.09.009.
[6] A.E. Hughes, A. Boag, A.M. Glenn, D. McCulloch, T.H. Muster, C. Ryan, C. Luo, X. Zhou, G.E. Thompson, Corrosion of AA2024-T3 Part II: co-operative corrosion, Corros. Sci. 53 (2011) 27–39, doi:10.1016/j.corsci.2010.09.030.
[7] W.J. Clark, J.D. Ramsey, R.L. McCreery, G.S. Frankel, A galvanic corrosion approach to investigating chromate effects on aluminium alloy 2024-T3, J. Electrochem. Soc. 149 (2002) 179–185.
[8] M. Bethencourt, F.J. Botana, J.J. Calvino, M. Marcos, M.A. Rodríguez-Chacón, Lanthanide compounds as environmentally-friendly corrosion inhibitors of aluminium alloys: a review, Corros. Sci. 40 (1998) 1803–1819.

[9] T.H. Muster, H. Sullivan, D. Lau, D.L.J. Alexander, N. Sherman, S.J. Garcia, T.G. Harvey, T.A. Markley, A.E. Hughes, P.A. Corrigan, A.M. Glenn, P.A. White, S.G. Hardin, J. Mardel, J.M.C. Mol, A combinatorial matrix of rare earth chloride mixtures as corrosion inhibitors of AA2024-T3: optimisation using potentiodynamic polarisation and EIS, Electrochim. Acta. 67 (2012) 95–103, doi:10.1016/j.electacta.2012.02.004.

[10] T.H. Muster, D. Lau, H. Wrubel, N. Sherman, A.E. Hughes, T.G. Harvey, T. Markley, D.L.J. Alexander, P.A. Corrigan, P.A. White, S.G. Hardin, M.A. Glenn, J. Mardel, S.J. Garcia, J.M.C. Mol, An investigation of rare earth chloride mixtures: combinatorial optimisation for AA2024-t3 corrosion inhibition, Surf. Interface Anal. 42 (2010) 170–174.

[11] A.E. Hughes, D. Ho, M. Forsyth, B.R.W. Hinton, Towards replacement of chromate inhibitors by rare earth systems, Corros. Rev. 25 (2007) 591–605.

[12] Y. Zhang, Y. Li, Y. Ren, H. Wang, F. Chen, Double-doped LDH films on aluminum alloys for active protection, Mater. Lett. 192 (2017) 33–35, doi:10.1016/j.matlet.2017.01.038.

[13] C.A. Drewien, M.O. Eatough, D.R. Tallant, C.R. Hills, R.G. Buchheit, Lithium-aluminum-carbonate-hydroxide hydrate coatings on aluminum alloys: composition, structure, and processing bath chemistry, J. Mater. Res. 11 (1996) 1507–1513, doi:10.1557/JMR.1996.0188.

[14] P. Visser, Y. Liu, H. Terryn, J.M.C. Mol, Lithium salts as leachable corrosion inhibitors and potential replacement for hexavalent chromium in organic coatings for the protection of aluminum alloys, J. Coatings Technol. Res. 13 (2016) 557–566, doi:10.1007/s11998-016-9784-6.

[15] P. Visser, H. Terryn, J.M.C. Mol, On the importance of irreversibility of corrosion inhibitors for active coating protection of AA2024-T3, Corros. Sci. 140 (2018) 272–285, doi:10.1016/j.corsci.2018.05.037.

[16] P. Visser, A. Lutz, J.M.C. Mol, H. Terryn, Study of the formation of a protective layer in a defect from lithium-leaching organic coatings, Prog. Org. Coatings. 99 (2016) 80–90, doi:10.1016/j.porgcoat.2016.04.028.

[17] X. Wang, F. Yang, G. Viswanathan, S. Wang, G.S. Frankel, Characterization and electrochemical assessment of Al-Zn-In alloy with trivalent chromium process coating, Corros. Sci. 176 (2020) 108933, doi:10.1016/j.corsci.2020.108933.

[18] X. Wang, G.S. Frankel, Transmission Line Modeling of Al-Rich Primer on AA2024-T3, J. Electrochem. Soc. 167 (2020) 081508, doi:10.1149/1945-7111/ab8e85.

[19] X. Wang, G.S. Frankel, Protection Mechanism of Al-Rich Epoxy Primer on Aluminum Alloy 2024-T3, Corrosion 73 (2017) 1192–1195.

[20] X. Wang, G.S. Frankel, The Effect of Trivalent Chromium Process on Al-Zn-In Pigments in Epoxy Primer on the Corrosion Protection of AA2024-T3, Corrosion 76 (2020) 103–113.

[21] E.L. Ferrer, A.P. Rollon, H.D. Mendoza, U. Lafont, S.J. Garcia, Double-doped zeolites for corrosion protection of aluminium alloys, Microporous Mesoporous Mater 188 (2014) 8–15, doi:10.1016/j.micromeso.2014.01.004.

[22] A.M. Glenn, T.H. Muster, C. Luo, X. Zhou, G.E. Thompson, A. Boag, A.E. Hughes, Corrosion of AA2024-T3 Part III: propagation, Corros. Sci. 53 (2011) 40–50, doi:10.1016/j.corsci.2010.09.035.

[23] D.A. Jones, Principles and Prevention of Corrosion, 2nd ed., Prentice Hall, New Jersey, USA, 1996.

[24] R.L. De Rosa, D.A. Earl, G.P. Bierwagen, Statistical evaluation of EIS and ENM data collected for monitoring corrosion barrier properties of organic coatings on Al-2024-T3, Corros. Sci. 44 (2002) 1607–1620.

[25] T. Breugelmans, J. Lataire, T. Muselle, E. Tourwé, R. Pintelon, A. Hubin, Odd random phase multisine electrochemical impedance spectroscopy to quantify a non-stationary behaviour: theory and validation by calculating an instantaneous impedance value, Electrochim. Acta. 76 (2012) 375–382, doi:10.1016/j.electacta.2012.05.051.

[26] A. Hubin, H. Terryn, J.M.C. Mol, M. Meeusen, P. Visser, L. Fern, The use of odd random phase electrochemical impedance spectroscopy to study lithium-based corrosion inhibition by active protective coatings, 278 (2018) 363–373. https://doi.org/10.1016/j.electacta.2018.05.036.

[27] P.J. Denissen, A.M. Homborg, S.J. Garcia, Interpreting Electrochemical Noise and Monitoring Local Corrosion by Means of Highly Resolved Spatiotemporal Real-Time Optics, J. Electrochem. Soc. 166 (2019) C3275–C3283, doi:10.1149/2.0341911jes.

[28] A.M. Homborg, E.P.M. van Westing, T. Tinga, X. Zhang, P.J. Oonincx, G.M. Ferrari, J.H.W. de Wit, J.M.C. Mol, Novel time–frequency characterization of electrochemical noise data in corrosion studies using Hilbert spectra, Corros. Sci. 66 (2013) 97–110, doi:10.1016/j.corsci.2012.09.007.

[29] A.M. Homborg, T. Tinga, X. Zhang, E.P.M. Van Westing, P.J. Oonincx, G.M. Ferrari, J.H.W. De Wit, J.M.C. Mol, Transient analysis through Hilbert spectra of electrochemical noise signals for the identification of localized corrosion of stainless steel, Electrochim. Acta. 104 (2013), doi:10.1016/j.electacta.2013.04.085.

[30] K. Hladky, J.L. Dawson, The measurement of localized corrosion using electrochemical noise, Corros. Sci. 21 (1981) 317–322.

[31] K. Hladky, J.L. Dawson, The measurement of corrosion using electrochemical 1/f noise, Corros. Sci. 22 (1982) 231–237.

[32] A.M. Homborg, T. Tinga, E.P.M. Van Westing, X. Zhang, G.M. Ferrari, J.H.W. de Wit, J.M.C. Mol, A Critical Appraisal of the Interpretation of Electrochemical Noise for Corrosion Studies, Corrosion. 70 (2014) 971–987, doi:10.5006/1277.

[33] T. Hagyard, J.R. Williams, Potential of aluminium in aqueous chloride solutions, Part 1, Trans. Faraday Soc. 57 (1961) 2288–2294.

[34] P.J. Denissen, S.J. Garcia, Reducing subjectivity in EIS interpretation of corrosion and corrosion inhibition processes by in-situ optical analysis, Electrochim. Acta. 293 (2019) 514–524, doi:10.1016/j.electacta.2018.10.018.

[35] S. Ritter, F. Huet, R.A. Cottis, Guideline for an assessment of electrochemical noise measurement devices, Mater. Corros. 61 (2010) 1–6, doi:10.1002/maco.201005839.

[36] A.M. Homborg, R.A. Cottis, J.M.C. Mol, An integrated approach in the time, frequency and time-frequency domain for the identification of corrosion using electrochemical noise, Electrochim. Acta. 222 (2016) 627–640, doi:10.1016/j.electacta.2016.11.018.

[37] A.M. Homborg, P.J. Oonincx, J.M.C. Mol, Wavelet Transform Modulus Maxima and Holder Exponents Combined with Transient Detection for the Differentiation of Pitting Corrosion Using Electrochemical Noise, Corrosion. 74 (2018) 1001–1010.

[38] M. Olgiati, P.J. Denissen, S.J. Garcia, When all intermetallics dealloy in AA2024-T3: quantifying early stage intermetallic corrosion kinetics under immersion, Corros. Sci. 192 (2021) 109836, doi:10.1016/j.corsci.2021.109836.

[39] C. Cai, Z. Zhang, F. Cao, Z. Gao, J. Zhang, C. Cao, Analysis of pitting corrosion behavior of pure Al in sodium chloride solution with the wavelet technique, J. Electroanal. Chem. 578 (2005) 143–150.

[40] A.M. Homborg, E.P.M. Van Westing, T. Tinga, G.M. Ferrari, X. Zhang, J.H.W. De Wit, J.M.C. Mol, Application of transient analysis using Hilbert spectra of electrochemical noise to the identification of corrosion inhibition, Electrochim. Acta. 116 (2014), doi:10.1016/j.electacta.2013.11.084.

[41] E.A. Matter, S. Kozhukharov, M. Machkova, V. Kozhukharov, Comparison between the inhibition efficiencies of Ce(III) and Ce(IV) ammonium nitrates against corrosion of AA2024 aluminum alloy in solutions of low chloride concentration, Corros. Sci. 62 (2012) 22–33, doi:10.1016/j.corsci.2012.03.039.

[42] S.J. García, T.H. Muster, Ö. Özkanat, N. Sherman, A.E. Hughes, H. Terryn, J.H.W. de Wit, J.M.C. Mol, The influence of pH on corrosion inhibitor selection for 2024-T3 aluminium alloy assessed by high-throughput multielectrode and potentiodynamic testing, Electrochim. Acta. 55 (2010) 2457–2465, doi:10.1016/j.electacta.2009.12.013.

[43] A.J. Davenport, H.S. Isaacs, M.W. Kendig, XANES Investigation of the role of cerium compounds as corrosion inhibitors for aluminum, Corros. Sci. 32 (1991) 653–663.

[44] P. Campestrini, H. Terryn, A. Hovestad, J.H.W. de Wit, Formation of a cerium-based conversion coating on AA2024: relationship with the microstructure, Surf. Coat. Technol. 176 (2004) 365–381.

[45] S.J. Garcia, T.A. Markley, J.M.C. Mol, A.E. Hughes, Unravelling the corrosion inhibition mechanisms of bi-functional inhibitors by EIS and SEM-EDS, Corros. Sci. 69 (2013) 346–358, doi:10.1016/j.corsci.2012.12.018.

[46] A. Kosari, M. Ahmadi, F. Tichelaar, P. Visser, Y. Gonzalez-Garcia, H. Zandbergen, H. Terryn, J.M.C. Mol, Dealloying-Driven Cerium Precipitation on Intermetallic Particles in Aerospace Aluminium Alloys, J. Electrochem. Soc. 168 (2021) 041505, doi:10.1149/1945-7111/abf50d.